Silicon (2022) 14:9499–9515
https://doi.org/10.1007/s12633-021-01521-6

ORIGINAL PAPER

Microstructure and Mechanical Property Correlation of Mg-Si Alloys

K. K. Ajith Kumar[1,2,3] · **A. Srinivasan**[2] · **U. T. S. Pillai**[2] · **B. C. Pai**[2] · **M. Chakraborty**[3]

Received: 14 September 2021 / Accepted: 1 November 2021 / Published online: 30 January 2022

Abstract

The present work aims at understanding the microstructure and mechanical property correlation of hypo (Mg-0.5, 0.7, 1.15 wt% Si) and hyper (Mg-2, 4, 6, 8 and 10 wt% Si) eutectic binary Mg-Si alloys. The microstructures of hypoeutectic alloys consist of α-Mg and lamellar Mg-Mg_2Si eutectic phases; whereas the microstructures of hypereutectic alloys consist of primary Mg_2Si, Chinese script eutectic Mg_2Si and α-Mg phases depending upon the Si content. Significant increase in hardness values of these alloys was observed as a function of Si content which is due to the presence of hard Mg_2Si phase. In the hypereutectic alloys, the average microhardness of primary Mg_2Si was about ten times higher than that of α-Mg. Compressive behaviour, tensile properties (UTS, YS and %E) at the room temperature (RT) as well as at 150 °C, elevated temperatures (ET) were analyzed and reported as follows: compressive strength of Mg-Si alloys has improved with the increase of Si content, Mg with 2 to 4 % Si shows good tensile properties at RT and ET. Alloys containing high Si content show a marginal reduction in strength at high temperatures due to the presence of the thermally stable Mg_2Si.

Keywords Mg-Si alloys · Casting and solidification · Mg_2Si · Hardness · Mechanical properties

1 Introduction

Nowadays, the design and development of 'safer, lighter and cleaner' vehicles are the subjects of worldwide energy-efficient research. In recent years, the aerospace and automobile industries have shown an increasing demand for novel thermo-mechanically reliable light materials for the overall weight-reduction which in turn limit the exhaust CO_2 emissions as per the legislative requirements [1–8]. Magnesium, with a density of 1.7 g/cc, which is two-third of the density of aluminium (2.7 g/cc) and one fourth of the density of steel (7.8 g/cc), is the lightest of the structural materials [1]. Mg alloys have an excellent specific strength, stiffness, dimensional stability, high damping capacity and recyclability. Most of the commercially used Mg alloys such as AZ91 (Mg-Al-Zn), AM50/60 (Mg-Al-Mn) and AS21/41(Mg-Al-Si) have reasonably high Al content and are the most economically competitive alloys [9–17]. They offer a combination of excellent castability, good corrosion resistance, reasonable room temperature strength and high ductility [18]. Their use in the automobile and electronic industries is restricted to relatively low-temperature applications. They are also unsuitable for power train applications in the automobile industry due to their poor mechanical properties at ET [19–21]. This is due to the presence of $Mg_{17}Al_{12}$ intermetallic in these alloys, which limits their strength and creep properties at ET [22, 23]. Hence, the development of low Al or Al free Mg alloys suitable for ET applications have been seriously considered and research attempts are underway.

Mg-alloys added with elements such as Ag [24, 25], Zr [26], Y [27] and rare earth (RE) [28–30] show good mechanical strength and creep resistance at ET. However, the use of such elements is uneconomical for fabricating high performance structural components. This situation opens the door for the development of low cost, thermally stable Mg-based alloys [8]. Silicon (Si) being a cheap element has long been used as an alloying element in Mg alloys to improve the ET properties [31]. Currently, the Mg-Si alloys containing in-situ intermetallic Mg_2Si have shown great potential as structural

---

✉ K. K. Ajith Kumar
ajithkajith@gmail.com

[1] Chief Executive Officer, MatRICS: Materials Research and Innovation Centric Solutions, Kanyakumari Dist., Vellimalai, Tamilnadu, India

[2] Materials Science and Technology Division, CSIR-National Institute for Interdisciplinary Science & Technology (NIIST), Thiruvananthapuram 695019, India

[3] Department of Metallurgical and Materials Engineering, Indian Institute of Technology Kharagpur, Kharagpur 721302, India

materials [32]. The maximum solid solubility of Si in Mg is only 0.003 at%, and Si atoms react with Mg atoms and precipitate as Mg_2Si intermetallic. The stable Mg_2Si that exists at stoichiometric composition exhibits high melting temperature (1085 °C), low density (1.99×10^3 kg/m^3), high hardness (4.5×10^9 N/m^2), low thermal expansion coefficient (7.5×10^{-6} K^{-1}) and reasonably high elastic modulus (120 GPa) which contributes to the improvement of mechanical properties, heat resistance and wear resistance of the Mg-Si alloys [33–37].

Several researchers have reported that the addition of Si elements in Mg-Al alloys such as AS21 and AS41 alloys, as the minor alloying element for die casting applications. These alloys are developed in the 1970 s and AS42 alloy was produced in the late 1980's. Although these alloys were significantly creeping resistant, they did not meet the requirements on transmission parts due to their poor casting and mechanical properties [38]. Mg_2Si intermetallic has many advantageous properties, but the binary Mg-Si based alloys for sand or permanent mold cast applications were not explored.

Elevated temperature mechanical properties and high strain rate superplasticity in Mg-Si alloys were also investigated by Mabuchi et al. [32, 39, 40]. They have studied the Mg-Si alloys with various amount of Si additions and reported that the alloys with low Si contents (< 10 wt%) showed higher values of the ultimate tensile strength than that of an alloy having higher Si contents (≥ 10 wt%) between 20 and 100 °C. Moreover, they have also reported that rapid solidified (RS) Mg-Si alloys show higher strength of 500 MPa at RT and superplastic behaviour at a high strain rate of 10^{-1}~1 S^{-1}at 500 °C [40]. However, a complete understanding of the structural property correlation of Mg-Si alloys is essential for the further development of these alloys. Therefore, the present work is taken up with the aim to investigate the microstructural and mechanical properties of various Mg-Si alloys.

Table 1 Holding temperature and time for various Mg-Si alloy composition

Mg-Si alloy	Holding temperature (°C)	Holding time (Min.)
Pure Mg	720	15
Mg-0.5Si	725	30
Mg-0.7Si	730	45
Mg-1.15Si	735	60
Mg-2Si	750	75
Mg-4Si	840	135
Mg-6Si	880	195
Mg-8Si	930	255
Mg-10Si	980	315

2 Experimental Details

Industrially pure magnesium ingot (99.7 %) and silicon lumps (99.5 %) were used as starting materials to prepare the Mg-Si alloys. Various compositions of these materials were melted separately in a low carbon steel crucible using a resistance furnace under a protective flux atmosphere. With reference to the Mg-Si phase diagram, different processing temperatures (750 to 890 °C) were maintained depending on the amount of Si addition for the complete dissolution of Si. For better dissolution, similar size range Si lumps were added together as a sandwich layer with Mg. Using this procedure, dissolution time and temperature of Mg-Si alloys were standardized. The melt was stirred which helped in dissolving the Si lumps uniformly in the melt. The holding temperature was always kept at 100 °C above the liquidus temperature for the respective compositions of Mg-Si alloys, which was obtained from the Mg-Si phase diagram (Fig. 1). The holding time was also standardized as 15 min for every 0.5 % Si addition. The standardized time and temperature were obtained by carrying out a number of trial experiments. The holding temperature and time for various Mg-Si alloy compositions are given in Table 1.

Later, the melt was poured into a preheated (350ºC) rectangular steel mold having dimensions 250mm×200mm×30mm. Castings of pure Mg and Mg alloys containing different Si (0.5, 0.7, 1.15, 2, 4, 6, 8 and 10 wt%) contents were prepared. Samples for material characterization such as optical microscopy, hardness, tensile, compressive were machined out from the same location of all the castings as per the ASTM Standards. For microstructural analysis, samples were etched using picric acid-based etchant (Picric acid – 6 g, Acetic acid – 5 ml, Ethanol – 100ml, Distilled water – 10 ml). Phase analysis and

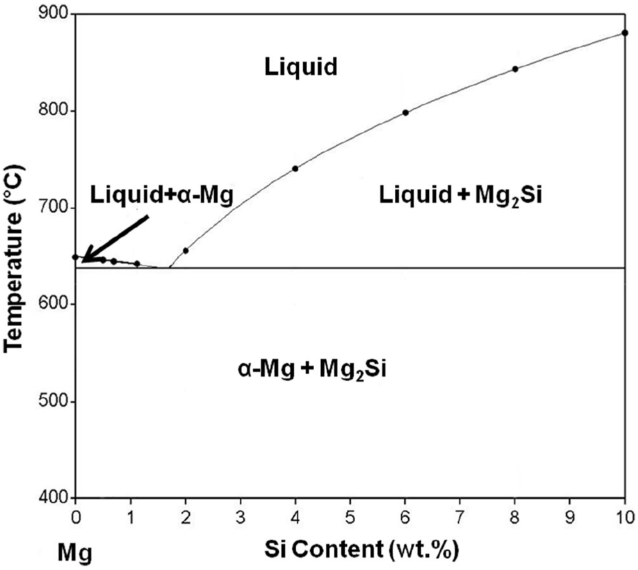

Fig. 1 Expanded Mg-Si phase diagram up to 10 wt% [29]

microstructural observation were carried out using X-ray diffractometer (PHILIPSPW1710) and optical microscopy (Leitz-Metalloplan). Quantitative microstructural analysis was carried out using a Leica 2001 image analyzer in conjunction with the optical microscope. The fields of observation were selected randomly at different locations of the sample. The sizes of different phases were measured manually. For each case, at least ten fields were analyzed from a single specimen and the average value is reported. To identify the type of precipitates on various castings the microstructural, tensile fracture and compressive fracture samples surface were examined using a JEOL, JSM 35 C scanning electron microscope with the operating voltage of 15-30 KeV.

Hardness measurements were carried out using Vickers hardness tester (Model: LV700, LECO Corporation, Michigan, U.S.A) to identify the hardness of the primary phase, eutectic region and the matrix of the Mg-Si alloys. Vickers hardness (macro) measurements were carried out using an indentation load of 5 kgf allowing a dwell time of 15 s for each indentation. The Vickers microhardness measurements were carried out on the polished samples using the fully automated CLEMEX microhardness tester. A 25gf constant load was maintained throughout the experiments with a 15 s dwell time. Average of ten indentations was taken for each specimen, and the scatter values were reported. RT and ET tensile tests were carried out using a computer-controlled INSTRON 8801 universal testing machine. Samples for tensile testing were prepared in accordance with the ASTM E8 standards. For HT testing, the samples were heated on an oven attached to the INSTRON machine and kept for 15 min after the required temperature was reached so as to ensure the homogenization of temperature throughout the sample. The compressive testing of the Mg-Si alloys were conducted at RT on a computer-controlled INSTRON 8801 Universal Testing Machine using the crosshead speed of 0.5 mm/min. Samples were machined as per ASTME9-09 standards.

3 Result and Discussion

3.1 XRD Analysis

Figure 2 shows the typical XRD patterns of Mg-Si alloys (Mg-1.15Si, Mg-6Si and Mg-10Si alloys). Only representative XRD patterns of hypo (Mg1.15Si) and hypereutectic (Mg-6Si, Mg-10Si) alloys are presented in this figure. XRD patterns of all the alloys show the peaks of Mg and Mg_2Si phases. The absence of Si peak indicates that all the added Si lumps completely reacted in the Mg melt forming Mg_2Si phase during solidification.

Table 2 gives the relative intensity of the major representative Bragg reflection of the Mg_2Si phases in Mg-Si alloys. It was found that with an increase in Si additions the relative intensity of all the peaks of Mg_2Si increases. This increase in intensity indicates that the quantity of Mg_2Si increases with an increase of Si content addition.

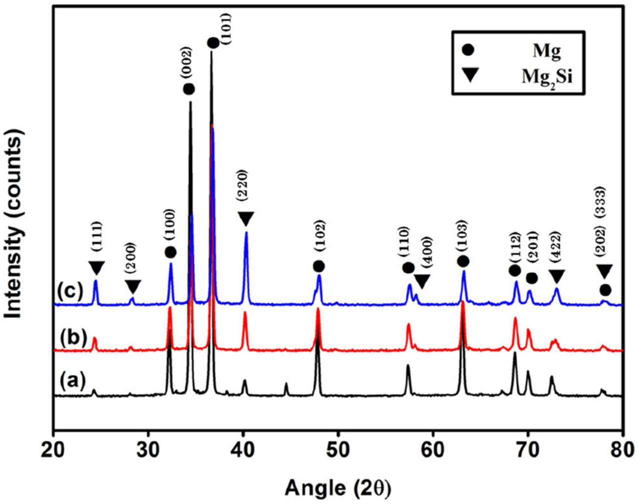

Fig. 2 XRD analysis of Mg-Si alloys (**a**) Mg-1.15Si, (**b**) Mg-6Si and (**c**) Mg-10Si

3.2 Microstructure

3.2.1 Hypoeutectic Mg-Si Alloys

Figure 3 presents the optical micrographs of pure Mg and different hypoeutectic Mg-Si (0.5, 0.7, 1.15Si) alloys. The microstructure of pure Mg (Fig. 3a), consists of single-phase Mg with a coarse grain structure. With 0.5 Si addition to Mg (Fig. 3b), the α-Mg grow as a dendritic structure and the eutectic forms in the inter-dendritic region. Similarly, Mg-0.7Si (Fig. 3c) and Mg-1.15Si (Fig. 3d) alloys also show dendritic α-Mg with lamellar eutectic structure.

To identify the phases present in the microstructure, as per the Mg-Si binary diagram [41], the eutectic equilibrium reaction on the Mg-rich side, $L \rightarrow Mg + Mg_2Si$, occurs at 637.6 °C at 1.34 wt% Si [42]. With an increase in Si content, the amount of the eutectic Mg_2Si phase increases and becomes coarse and continuous.

Table 2 Relative intensity of major representative Bragg diffraction of Mg_2Si

Sample detail	Relative intensity % (I/I_0) of *(h k l)*						
	(111)	(200)	(220)	(222)	(400)	(420)	(422)
Mg-1.15Si	1.84	0.56	4.65	-	-	27.18	-
Mg-6Si	5.96	1.1	16.89	0.53	2.79	21.81	4.91
Mg-10Si	13.76	3.21	40.35	0.33	5.61	18.61	9.29

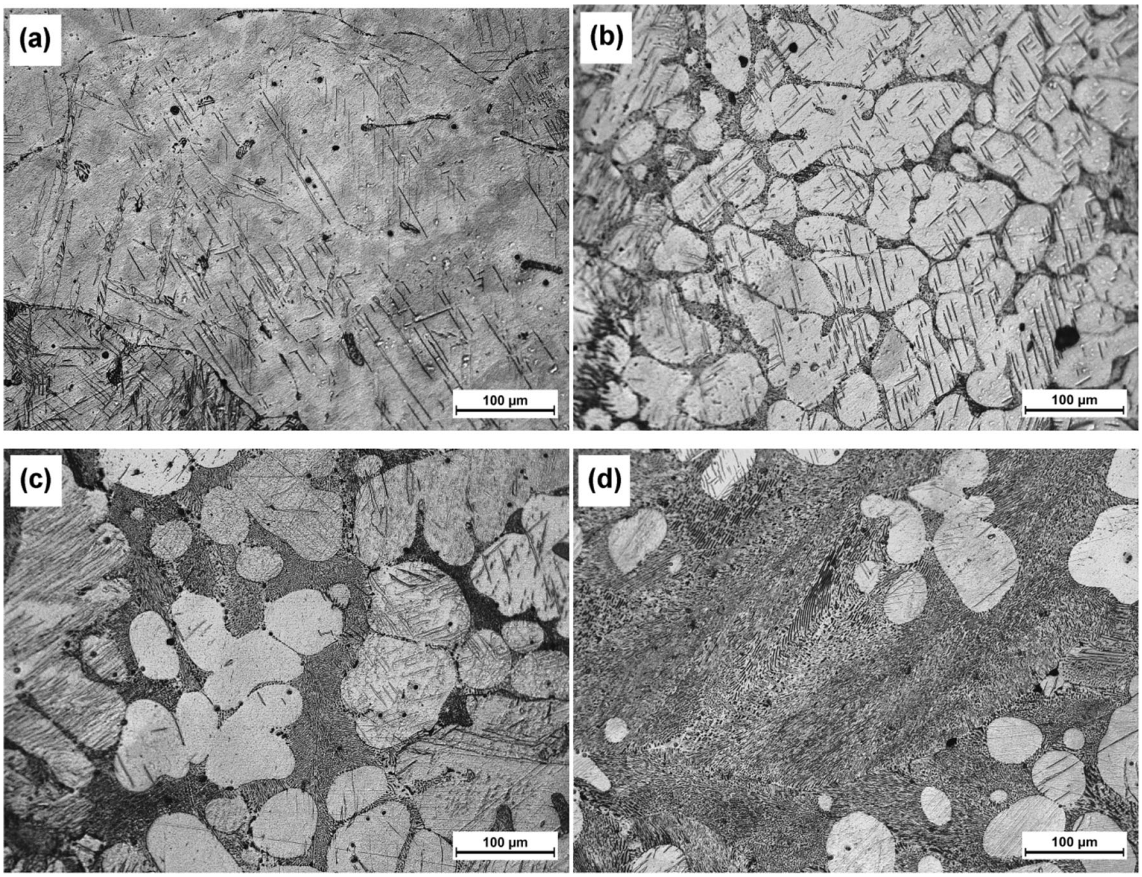

Fig. 3 Microstructures of (**a**) pure Mg, (**b**) Mg-0.5Si, (**c**) Mg-0.7Si and (**d**) Mg-1.15Si

SEM-EDS analyses on the different regions were carried out in Mg-1.15Si alloy (Fig. 4) and the results are shown in Table 3. Region A consists of 99.87 at% Mg and 0.13 at% Si, and therefore, it is confirmed as α-Mg phase. The region B has higher Si content (20.17 at%) and hence it is confirmed as eutectic Mg_2Si. The region C is the inter-lamellar region which has 4.53 at% Si and is eutectic α-Mg.

Similarly, the amount of α-Mg gets reduced as the Si content increases. In the hypoeutectic Mg-Si alloys, the eutectic grows in a lamellar manner from the solid α-Mg phase surface. As the α-Mg phase solidifies, excess Si diffuses on a short distance laterally where it is incorporated in the Si-rich Mg_2Si phase. Similarly, the Mg atoms rejected ahead of the Mg_2Si diffuse to the tip of

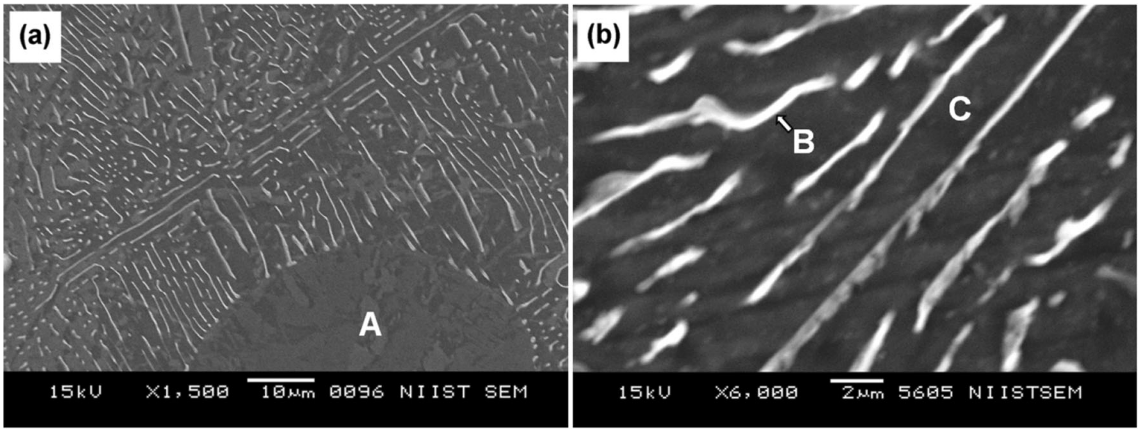

Fig. 4 SEM micrograph of Mg-1.15Si alloy indicating regions A, B and C selected for EDS analyses. (**a**) Low magnification micrograph and (**b**) High magnification micrograph

Table 3 EDS analyses of regions A, B and C marked in Fig. 4 (Weight and atomic fraction %)

Element/Regions	MgK		SiK	
	wt%	at%	wt%	at%
A	99.85	99.87	0.15	0.13
B	79.83	83.49	20.17	16.51
C	95.48	96.06	4.53	3.94

the adjacent α-Mg lamella and hence a lamellar eutectic forms [43].

The interlamellar spacing of eutectic Mg-Mg_2Si regions is measured using image analyses software and is shown in Fig. 5. It can be seen that interlamellar spacing increases with an increase in Si content in the hypoeutectic alloys.

3.2.2 Hypereutectic Mg-Si Alloys

Figure 6 shows the microstructures of different hypereutectic Mg-Si alloys (Mg-2 to 10Si). In general, the microstructures of these hypereutectic alloys consist of black polygonal/dendritic shaped particles surrounded by white regions containing needle/Chinese script like phases.

Figure 7 represents the SEM-EDS analyses carried out on different regions A, B, and C to identify the phase present in the alloy. The EDS analyses results of the marked regions are presented in Table 4.

The region A consists of 34.27 at% Si and 65.73 at% Mg, which suggests that it is the primary Mg_2Si phase. The primary α-Mg (region B) consists of a very little amount of Si (0.13 at%). Region C has 22.09 at% Si and it is known as eutectic Mg_2Si. However, the Si content present in the eutectic Mg_2Si is less than that of the primary Mg_2Si. This is due to the occurrence of an error during EDS measurements; the error occurred because the penetration depth of the electron beam is higher than the thickness of the eutectic Mg_2Si. From the result, it can be concluded that the black colour polygonal phase is primary Mg_2Si and the white surrounding region is α-Mg. It is apparent from the microstructure (Fig. 6a) that the needle/lamellar shape phase is eutectic Mg_2Si. It is observed that most of the α-Mg is seen around the primary Mg_2Si phase and the size of the primary Mg_2Si varies from 5 to 25 µm. When the Si addition increases to 4 %, the size and volume of the primary Mg_2Si also get increased (Fig. 6b). The morphology of eutectic Mg_2Si changes from the long needle/lamellar to Chinese script type structure. When Si addition is further increased to 6 % most of the primary Mg_2Si is converted to dendritic structure (Fig. 6c). In eutectic phase the Chinese script morphology of Mg_2Si is more apparent. As the Si content increases further to 8 %, and 10 % the primary Mg_2Si become coarser and dendritic (Fig. 6d and e). In addition, the amount of eutectic Mg_2Si also decreases with an increase in Si content in hypereutectic alloys. The size of the primary Mg_2Si particle in Mg-Si alloys was measured using image analysis software (Fig. 8). The average of the longest and shortest dimension of the particles was considered for the size measurement because the particles have no definite shape.

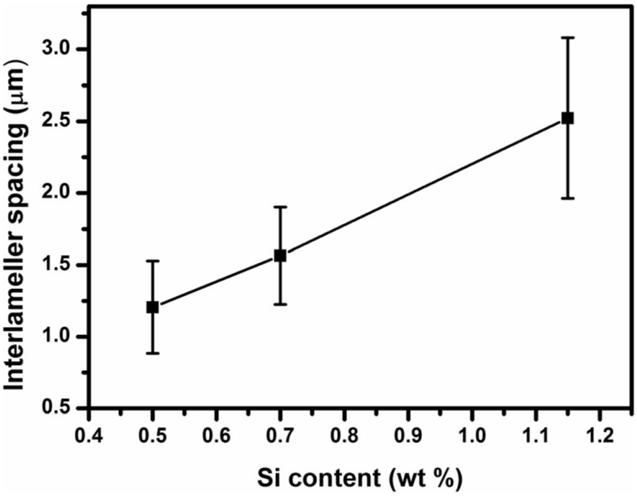

Fig. 5 Interlamellar spacing of different hypoeutectic Mg-Si alloys

In case of dendrites (Mg-6 to 10 Si alloy), the primary dendritic arm size is taken as the size of the Mg_2Si. Difficulties were encountered during the measurement of the dendrite size as the microstructure consists of different dendrite lengths, and hence large deviation in size was observed on high Si alloys (Fig. 6d and e). The volume percentage of the primary Mg_2Si estimated using image analysis software and the theoretical percentage obtained from Pandat software are shown in Fig. 9. The results clearly show that the Mg_2Si content increases with an increase in Si content in the alloys which is in line with the microstructural observation.

Figure 10 shows the schematic representation of the microstructural development of hypereutectic Mg-Si alloys during solidification. According to the Mg-Si binary equilibrium phase diagram, the hypereutectic Mg-Si alloys would solidify resulting in a microstructure comprising of primary Mg_2Si and eutectic Mg-Mg_2Si. The solidification path is indicated as follows [39]. During solidification, the first phase precipitating from the liquid melt is the primary Mg_2Si and then the rest of the melt solidifies as a binary eutectic structure consisting of α-Mg and eutectic Mg_2Si. The schematic diagram of primary and eutectic growth of Mg_2Si is presented in Fig. 11a-c. During growth, the primary Mg_2Si consumes Si atoms from the surrounding liquid and hence the Si depleted liquid forms around it and reaches the composition of α-Mg. When the temperature drops to 650 °C, the α-Mg solidifies surrounding

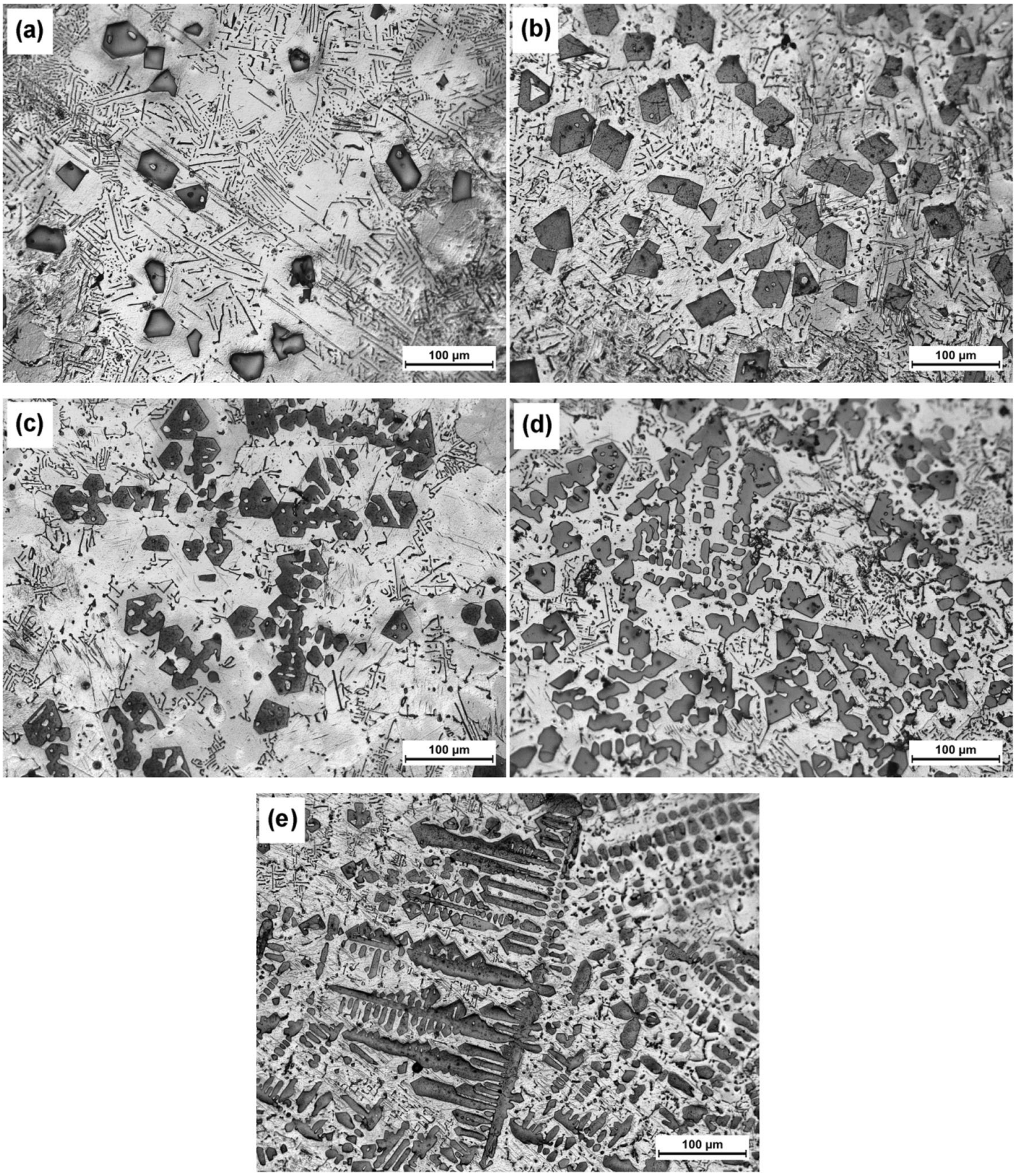

Fig. 6 Microstructures of hypereutectic Mg-Si alloys (**a**) Mg-2Si, (**b**) Mg-4Si, (**c**) Mg-6Si, (**d**) Mg-8Si and (**e**) Mg-10Si

the primary Mg_2Si. The remaining liquid melt, which is near or equal to the eutectic composition, will solidify as eutectic Mg_2Si at 637 °C as shown in Eq. 1.

$$L \rightarrow L1 + Mg_2Si \rightarrow Mg_2Si + (Mg - Mg_2Si)_{\text{eutectic}} \quad (1)$$

The formation of above microstructure feature is mainly attributed to the solidification of the alloy under relatively high cooling rate, leading to deviation from the equilibrium diagram during solidification. Hence, under non-equilibrium condition, such as in the case of ingot metallurgy, the solidification path is indicated as in the Eq. 2 [44].

$$L \rightarrow L1 + Mg_2Si \rightarrow L_2 + Mg_2Si + \alpha - Mg \rightarrow Mg_2Si + \alpha - Mg + (Mg - Mg_2Si)_{\text{eutectic}} \quad (2)$$

Moreover with respect to Si addition, the morphology of the primary Mg_2Si also varies. From Figs. 10 and 11, it is noted that, for low Si-containing hypereutectic alloys, solidification starts at a lower temperature. For instance, in the case of Mg-2Si alloy, the primary Mg_2Si start solidifying at 657 °C. However, at higher Si content (Mg-10Si), the alloys starts solidifying at very high temperatures (880 °C) as

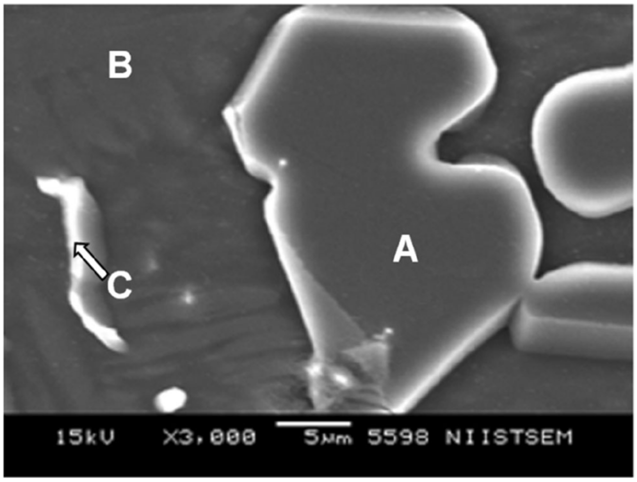

Fig. 7 SEM micrograph of Mg-2Si indicating regions A, B, and C selected for EDS analyses

compared to the lower Si added alloys. Therefore at higher addition the primary Mg_2Si gets more time to solidify thus showing the coarse dendritic type morphology. The morphology change of the primary Mg_2Si depends on the Si content in the alloy. Porter and Easterling, [43] have reported that other than dendritic morphology, primary Mg_2Si exhibits three typical morphologies: perfect, hopper and truncated octahedron. Because of the random cutting angles, a variety of polygonal outlines of primary Mg_2Si in the polished sections such as triangle, square, trapezoid and hexagon are observed [45]. Theoretically, the growth of primary Mg_2Si crystals follow a typical faceted growth pattern in conventional solidification conditions, owing to its high entropy of fusion and large Jackson's factor [45, 46]. The final morphology of the crystal is determined by the crystal structure, the crystal growth conditions and process. The internal factors lead to equilibrium crystal form with minimum total surface free energy. Various morphologies are developed when different external factors also influence crystal forms and force the crystal to deviate from the equilibrium form. The crystal shape is derived from the competition of these internal and external factors, and its growth is related to the growth kinetics, such as interface property, capillarity, heat and mass transfer. The eutectic Mg_2Si forms towards the end of solidification at 637 °C and it grows as a needle or Chinese script type morphology in the hypereutectic alloys. This is in sharp contrast to the lamellar type of eutectic growth seen in the case of the hypoeutectic Mg-Si alloys. The morphological change of eutectic constituent in hypereutectic alloys is probably due to the high range of non-equilibrium solidification (from liquidus to solidus) and insufficient amount of Si atom for coupled eutectic growth at the final stage of solidification.

Table 4 EDS analyses of region A, B and C

Regions marked in Fig. 7	Mg		Si	
	wt%	at%	wt%	at%
A	62.41	65.73	37.59	34.27
B	99.85	99.87	0.15	0.13
C	75.63	77.91	24.37	22.09

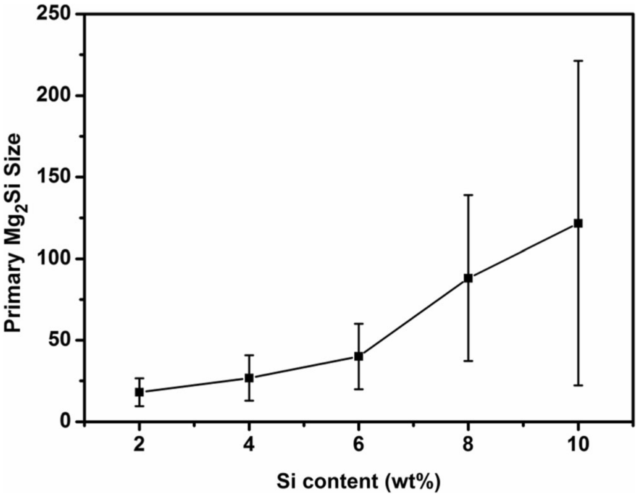

Fig. 8 Variation in size of the primary Mg_2Si particle with Si content

3.3 Mechanical Properties

3.3.1 Macrohardness

Figure 12 reveals the Vickers hardness of pure Mg and Mg-Si alloys. The hardness value steadily increases with an increase in Si content. The hardness of pure Mg increases from 30 HV5 to 72 HV5 with 10Si addition. The enhancement with an increase in the Si additions in hardness is due to the presence of hard Mg_2Si intermetallic phase. Moreover, increasing the

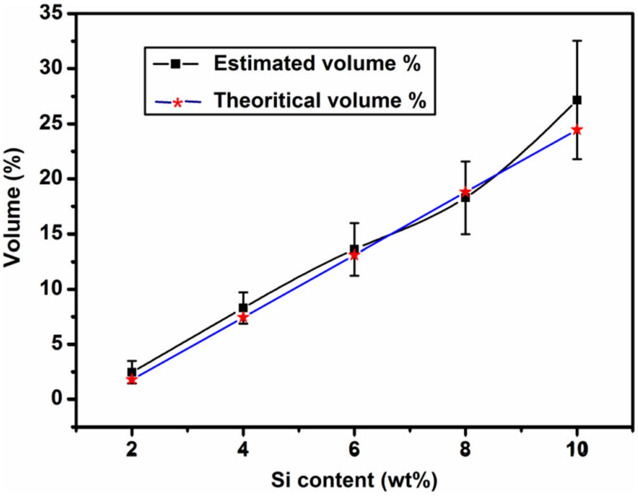

Fig. 9 Theoretical and estimated volume percentage of Mg_2Si in hypereutectic Mg-Si alloys

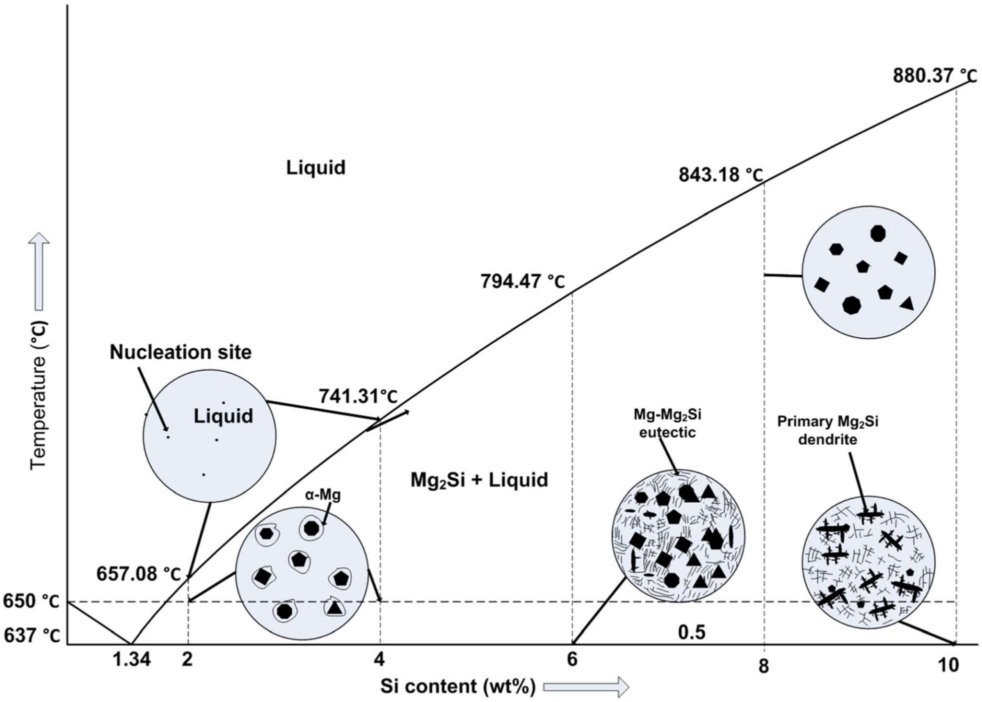

Fig. 10 Schematic representation of the microstructural development of hypereutectic Mg-Si alloys during solidification

volume of Mg_2Si with respect to Si addition increases the hardness. While comparing with hypo, the hypereutectic Mg-Si alloys have higher hardness, which is due to the presence of the hard and brittle primary Mg_2Si phase in the α-Mg matrix.

3.3.2 Microhardness

Indentation microhardness testing is a convenient technique to investigate the mechanical properties of a local, small volume of material. The Vickers microhardness (HV) is defined as in Eq. 3:

$$HV = 1.8544P/d^2 \tag{3}$$

Where P is the applied load and d is the indentation size. Figure 13 shows the Vickers microhardness of α-Mg, eutectic Mg-Mg_2Si and primary Mg_2Si phases present in both the hypo and hypereutectic Mg-Si alloys. It is noticed that the average hardness of the primary Mg_2Si (350 HV0.025) is about 10 times higher than that of α-Mg (32 HV0.025).

The hardness of α-Mg and eutectic Mg-Mg_2Si phase in different alloys do not change much in spite of the change in the eutectic morphology of the alloys. A relatively large variation in hardness is observed on the primary Mg_2Si phase alloy, which is mainly due to the encountered difficulties during measurement.

Micro indentation of the microhardness test are indicated in Fig. 14(a to d). Figure 14(a) represents the presence of low hardness α-Mg which is similar to pure Mg; the edges of the indentation are not sharp which indicate its ductility. The eutectic Mg-Mg_2Si region shows comparatively higher hardness than α-Mg in both the hypo and hypereutectic alloys (Fig. 14b). In hypereutectic alloys, the primary Mg_2Si phase exhibits the highest hardness among all the other constituents. Figure 14(c), (d) shows the primary Mg_2Si before and after indentation. For the same load on primary Mg_2Si, the indentation mark observed is very small and it produces crack at the corners indicating its brittle nature. The crystal structure of the stoichiometric Mg_2Si is diamond cubic, positioned by Si atoms, whereas the tetrahedral interstices are occupied by Mg atoms. Due to the restricted number of active slip systems Mg_2Si reveals an inherent brittleness up to the brittle-ductile transition temperature of about 450ºC [47].

3.3.3 Tensile Properties

Room Temperature (RT) The ultimate tensile strength (UTS), yield strength (YS) and the ductility (%E) values of different Mg-Si alloys at RT are shown in Fig. 15. The UTS values increase up to 2 % Si addition; beyond that, it decreases slightly (from 148 MPa to 139 MPa) in UTS is noticed with Mg-4Si alloy. However, the UTS value of Mg-6Si reduces drastically to 97 MPa which is even less than that of pure Mg (111 MPa) and thereafter, they do not change much. Even though the increase in YS up to 0.7Si is not significant, a gradual increase is noticed beyond that. The maximum YS is obtained for Mg-6Si alloy (77 MPa) and beyond that marginal reduction is observed. However, the YS of Mg-10Si alloy are higher than that of pure Mg. The ductility, as measured by the

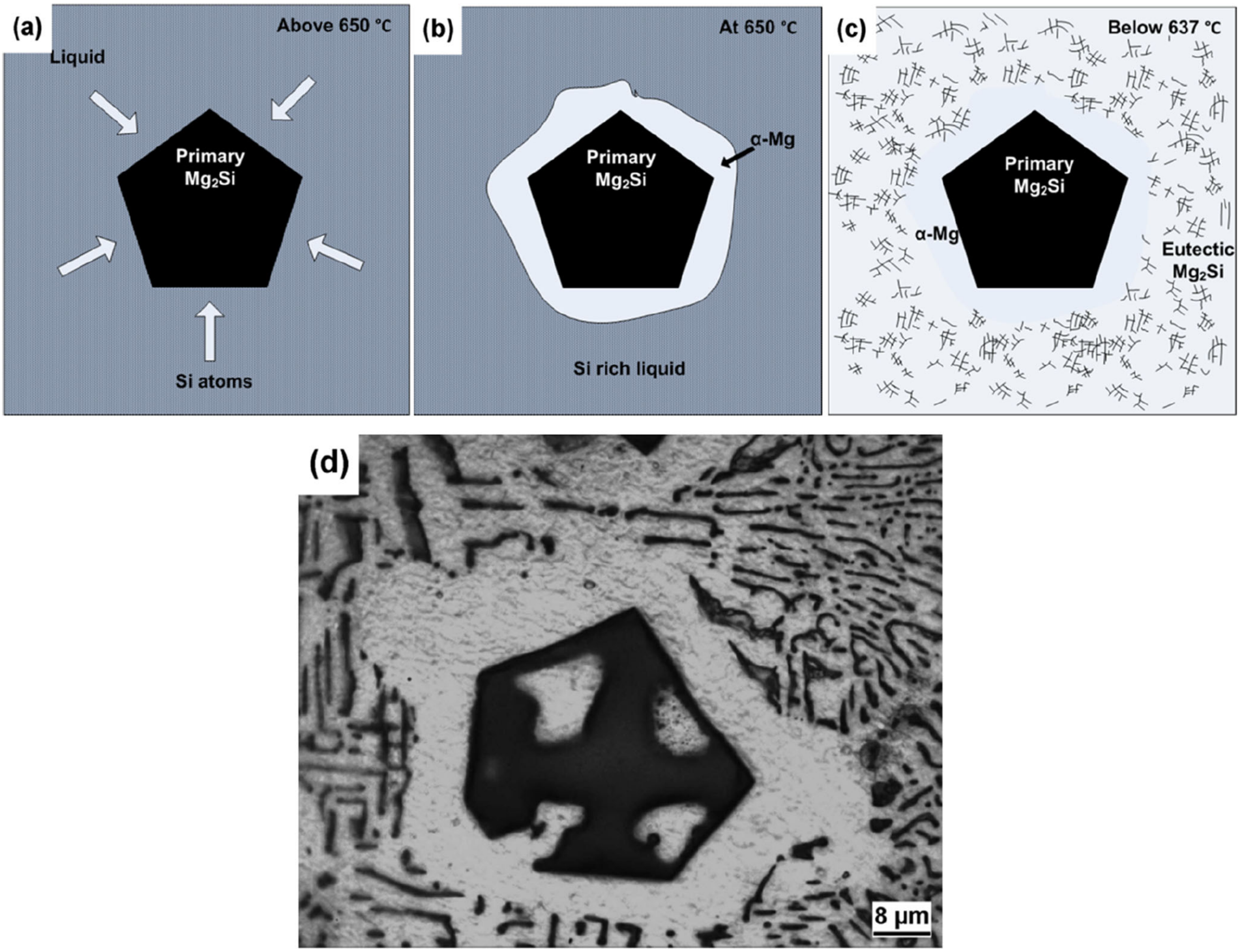

Fig. 11 Schematic representations of (**a**) primary Mg$_2$Si growth above 650 °C, (**b**) α-Mg growth surround the primary Mg$_2$Si at 650 °C (**c**) Eutectic Mg$_2$Si growth at 637 °C and (**d**) Typical microstructure Mg-4Si alloy

%E gradually decreases with Si additions. The ductility of Mg-10Si is 1.94 % whereas the ductility of pure Mg is 11.78 %.

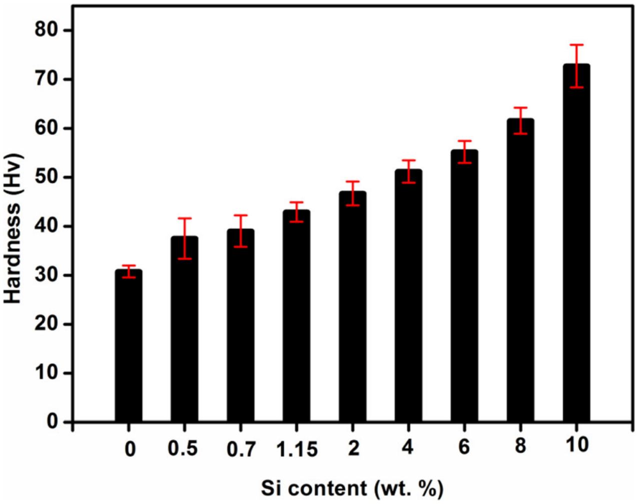

Fig. 12 Hardness of Mg-Si alloy with respect to Si content

The overall observation shows that Mg with 2 and 4 % Si provide better tensile properties. The uniform distribution of

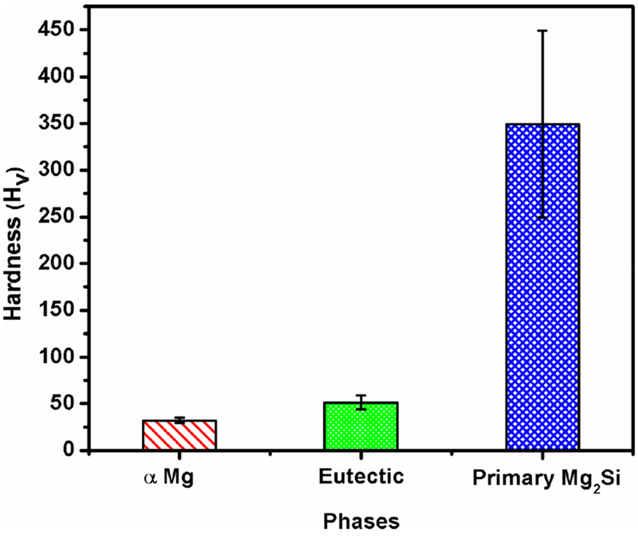

Fig. 13 Micro hardness (H_v) of Mg-Si alloy

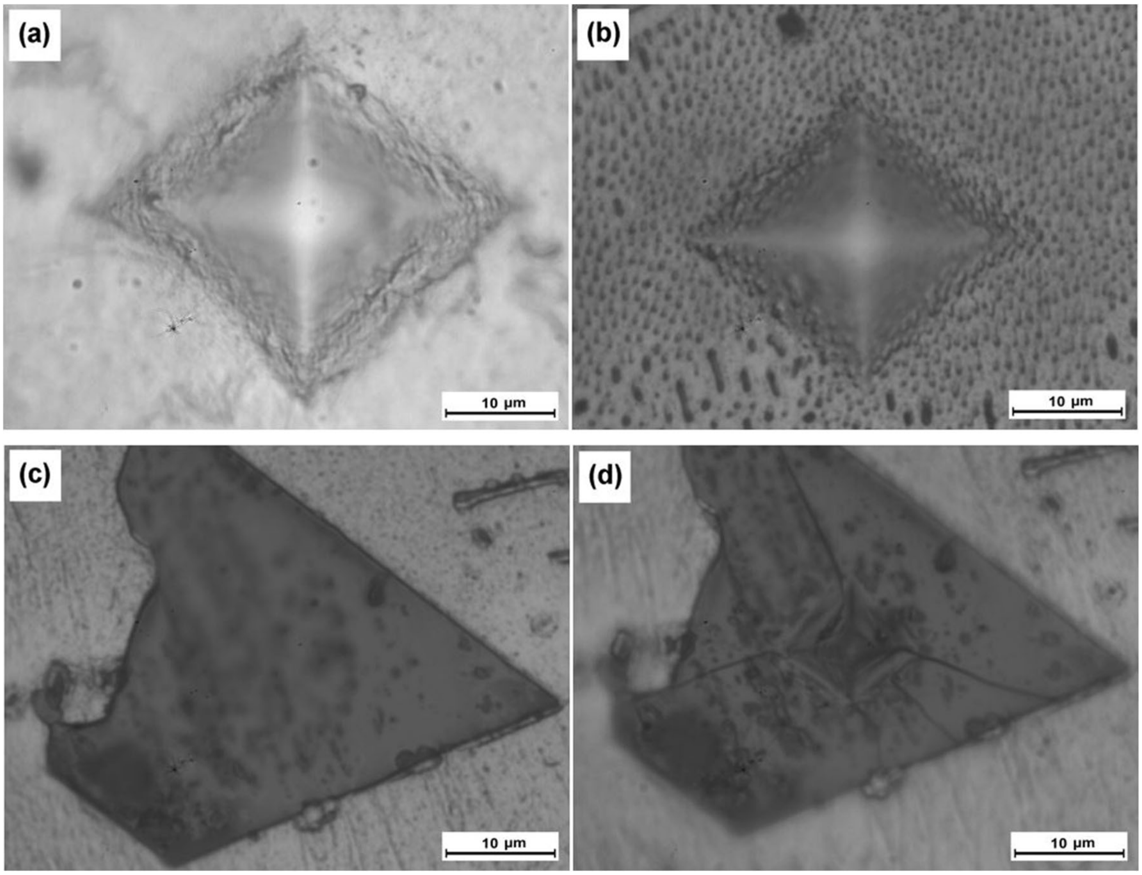

Fig. 14 Micro indentation on various phases in Mg-Si alloys (**a**) On α-Mg halos, (**b**) On Mg-Mg_2Si eutectic (**c**) Primary Mg_2Si phase before indentation and (**d**) Primary Mg_2Si after indentation

the fine eutectic and primary Mg_2Si phases distributed in the Mg matrix is attributed to the improvement in tensile properties. In general, the increase in UTS and YS in hypoeutectic alloys (up to 1.15Si) with an increase in Si content is attributed to the increase in the eutectic volume (Fig. 3b-d).

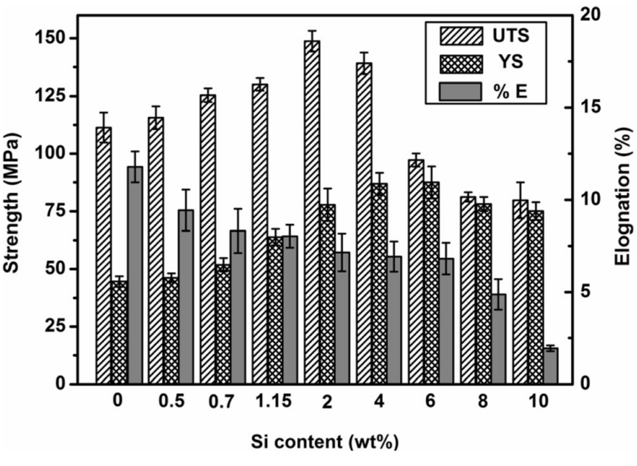

Fig. 15 Tensile properties of Mg-Si alloys tested at RT

The presence of the fine primary Mg_2Si, in addition to a eutectic constituent in hypereutectic alloys, provides high strength properties in Mg-2Si alloys. The reduction in strength properties with Mg-4Si and addition beyond that is due to the existence of high volume coarse dendrite shape primary Mg_2Si phase (Fig. 6c-e). The main factors that form fracture morphology in engineering materials are the relation between the external loading, cohesive force levels and the internal stresses in the crystallographic lattice at different ranges of interaction [48]. Figure 16 presents the typical RT tensile fracture surfaces of Mg-(0, 1.15, 6 and 10) Si alloys. The microfracture mechanisms observed on the tensile fractured surfaces using SEM reveals long cleavages indicating the brittle type of fracture in pure Mg. With HCP structure, the failure of Mg alloys is expected to be brittle through cleavage or quasi-cleavage fracture, as the slip systems in HCP at RT are limited. Fractograph of hypoeutectic Mg-1.15Si alloy (Fig. 16b) shows cleavage with river type patterns which indicates the brittle type of fracture. Energy is consumed for forming two new surfaces and to overcome the work on the cleavage planes. The river pattern represents the cracks propagating in the cleavage planes which require more energy. The commonly observed connections of the cleavage steps reflect the tendency for minimizing the fracture work along the crack path. This alloy contains mostly eutectic, consisting of an alternate lamellar layer of hard Mg_2Si and soft α-Mg. Initially crack nucleates in the hard lamellar Mg_2Si and then

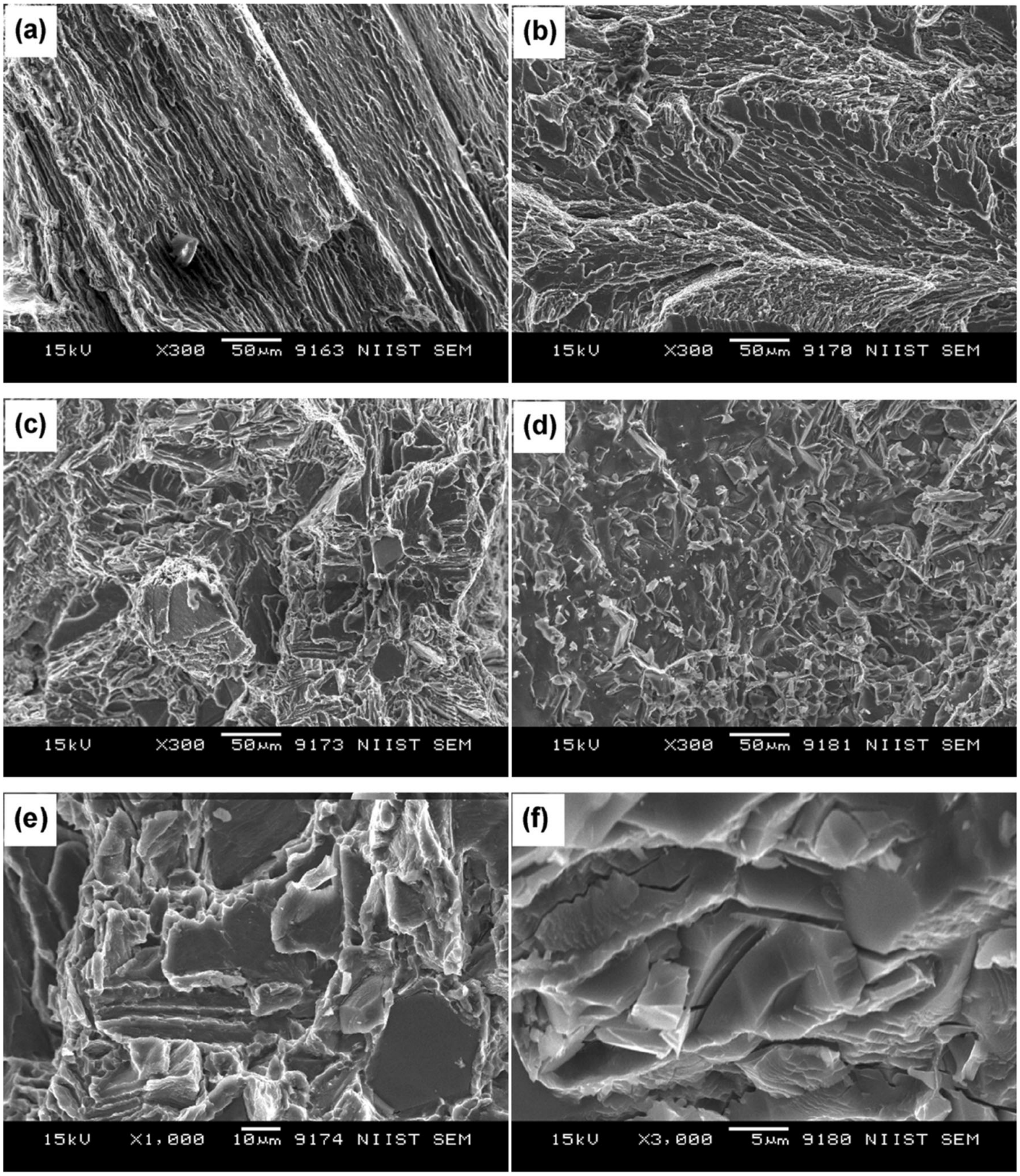

Fig. 16 Tensile fractograph of Mg-Si alloys tested at RT (**a**) pure Mg, (**b**) Mg-1.15Si (**c**)Mg-6Si, (**d**) Mg-10Si, (**e**) Cellular fracture surface of Mg-6Si alloy and (**f**) Brittle Mg_2Si dendrite in Mg-10Si alloy

propagates through the lamellar. The sharp edges or ends of the brittle Mg_2Si phases are preferred crack initiation and stress concentration sites [28, 49].

Figure 16c presents the fractograph of Mg-6Si alloy which shows many fractured particles of the primary Mg_2Si. Highly deformed regions around the brittle Mg_2Si particle, which are probably α-Mg, are also observed. The fracture planes of almost all the coarse primary Mg_2Si particles exhibit clear cleavage without river pattern indicating a rapid fracture deriving from their intrinsic brittleness and pre-cracked structure, which is known as cellular fracture surface. On the cellular fracture surface, the features of both brittle and ductile fracture are present simultaneously [50, 51], which are seen in the high magnified factograph presented in Fig. 16e. It is typical on the polyphase material, where the microstructure components have different mechanical behaviour. Due to the strong cohesion at the interfaces between α-Mg and Mg_2Si, the matrix is deformed under local active stress [51]. The formation of this kind of fracture demands higher energy input compared with brittle cracks. According to Emamy et al. [52], the energy is absorbed during plastic deformation, causing an activation of the slip systems in successive micro-regions, which is evident from the high yield strength in Mg-6Si alloy. The fractograph of Mg-10Si shown in Fig. 16d reveals many large sheared Mg_2Si particles which suggest that these particles play a major role during the fracture. The relatively clean exposed surfaces of the particles point to the fact that they have cleaved during the fracture process. Multiple cracked Mg_2Si particles noticed in Fig. 16d and f suggests that the Mg_2Si dendritic particles provide the sites for fracture initiation because of their large dendritic morphology. The fracture of the Mg_2Si is due to the stress concentration around it. Once the crack nucleates, it propagates at a faster rate, which reduces the ductility [39].

Elevated Temperature (ET) Tensile properties of Mg-Si alloys at 150ºC are shown in Fig. 17. In general, the strength properties of the alloys decrease with an increase in the testing temperature from RT to ET especially with low Si containing alloys (Figs. 15 and 17). However, in the high Si content (Mg-6, 8 and 10Si) alloys, the reduction in strength is very marginal. For instance, the average UTS of Mg-2Si alloy decreases from 148 MPa to 123 MPa (16.8 %) when the testing temperature increases from RT to ET, whereas the UTS of Mg-10Si reduces only from 79 MPa to 74 MPa (6.33 %). Normally in RT, the HCP structured Mg alloys exhibit brittle failure due to the limitations in slip systems; only basal slip is active at RT. However, at ET additional slip systems such as prismatic and pyramidal slip planes are active. Cross slip takes place through these planes at high temperatures and introduces more ductility [53].

The ET tensile fractographs are presented in Fig. 18. The improvement in the ductility of the alloys obtained at ET is correlated to the fracture surface. Figure 18a shows the fractograph of pure Mg tested at ET which significantly varies from that of the RT fractograph (Fig. 16). The ET fractograph of pure Mg has large amount of deformation with dimples along with few cleavages. The high magnification fractograph (Fig. 18e) of pure Mg at elevated temperature also shows more dimples and cleavage plane along the deformation zone. Figure 18b shows the ET fractograph of Mg-1.15Si which shows that, more cleavage facets are connected with tearing ridges and shallow dimples which ensures high elongation values obtained at 150 °C temperature. This is due to the introduction of additional slip planes such as pyramid and prismatic planes through which cross-slip takes place at ET. With 6Si addition, well-defined cleavage planes with Mg_2Si particle cracks and pullouts are observed in Fig. 18c, which is almost the same as RT fracture at 6Si alloy. When the Si content increases (Mg-10Si), the plastic zone in the Si added alloy is reduced due to the presence of coarse and brittle Mg_2Si particles, which makes the alloy more brittle (Fig. 18d). Also, decohesion of the Mg_2Si dendrites from the matrix has occurred in a few regions indicating that the interface between the matrix and Mg_2Si is relatively weak. Compared to fractograph of RT tested samples, more number of dendritic decohesion are observed at ET (Fig. 18d). Figure 18f shows the high magnified micrograph of cracked Mg_2Si in Mg-10Si alloy. The image clearly shows that the large crack observed along the dendrite, indicating that alloy failed in brittle manner even at ET.

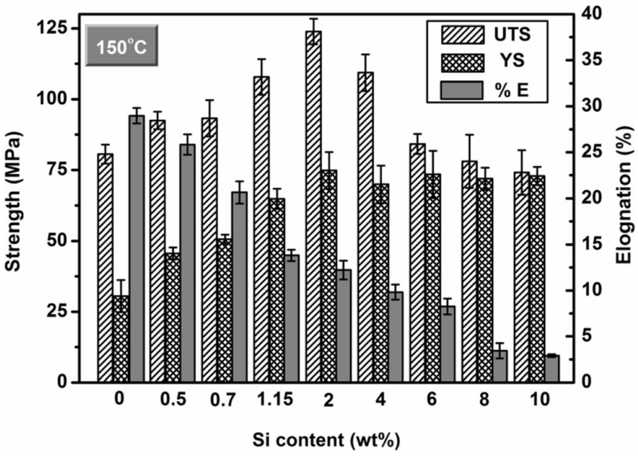

Fig. 17 Tensile properties of Mg-Si alloys tested at ET

3.3.4 Compressive Properties

Compression properties of different Mg-Si alloys were investigated and the ultimate compressive strength (UCS) values with varying Si content are shown in Fig. 19. The UCS of the alloy is found to increase significantly with an increase in Si content. For instance, the UCS of Mg-10Si is 283 MPa which is 35 % higher than that of pure Mg. This is due to the presence of the hard intermetallic Mg_2Si phase which shares the major load from the matrix. The fractographs of different Mg-Si alloys tested under compression load are presented in Fig. 20. Most of the Mg-Si alloy specimens tested in compression failed at an angle of 45° to the axis of loading which is in line with earlier observation [54].

In general, the fracture surfaces are shallow and flat, unlike those of tensile fracture. Figure 20a shows the compressive fracture surface of pure Mg at ambient temperature, which reveals a planar and smooth fracture surface, interspersed with some shallow ridges [55]. Smooth fracture surface indicates that pure Mg exhibits relatively more ductility compared to Si-added alloys [56]. This is also evident from the large spaced shear bands present on the fracture surface of pure Mg [56–58]. Shear bands are regions of distortion, where a portion of grain has rotated towards another orientation to accommodate the applied strain. When these regions extend across many grains they are called share bands. Exhaustive shear

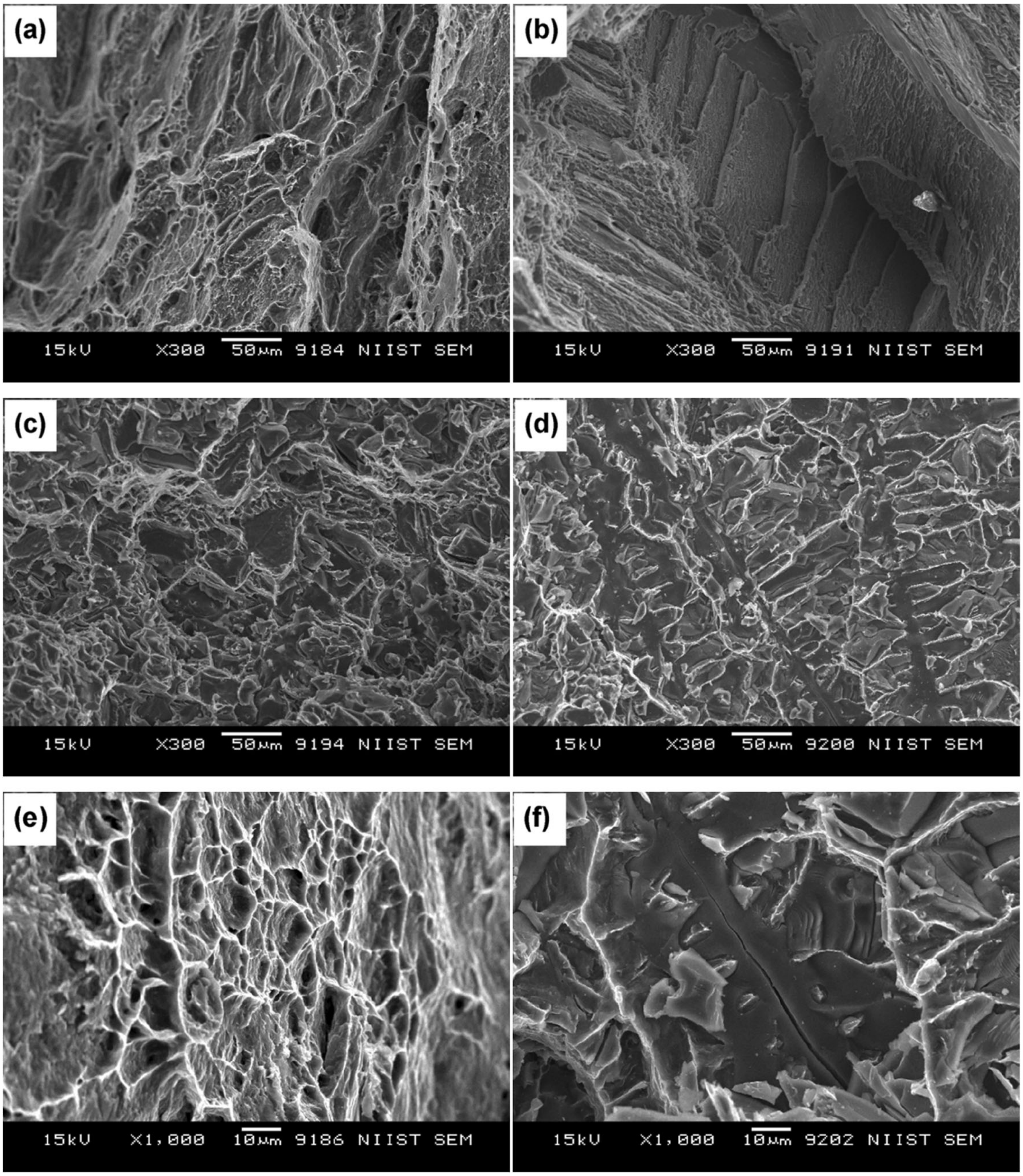

Fig. 18 Tensile factographs of Mg-Si alloys tested at ET (150 °C) (**a**) pure Mg, (**b**) Mg-1.15Si, (**c**) Mg-6Si, (**d**) Mg-10Si, (**e**) Ductile dimples of pure Mg and (**f**) cracking of Mg_2Si dendrite

along these bands is a common type of failure in pure metal [59].

The fractograph of Mg-1.15Si alloy shows shear bands with comparatively less spacing (Fig. 20b) (compared to that of pure Mg), which results in less ductility. The fracture surface of Mg-6Si is shown in Fig. 20c, in which the matrix is smeared by the Mg_2Si particle when being compressed. Particle fracture is not commonly observed it exhibits features that are consistent with the particles, having moved considerable distances before the final fracture [54]. In high Si samples (Mg-10Si) it is found that, fracture occurred after the maximum flow stress has reached without the softening stage; the surface experiences a typical brittle fracture. Microcracks are gradually generated and then propagated into the matrix or through the interface between Mg_2Si phase and Mg matrix. Finally, with a further increase in the load, the cracks propagate and cause total failure of the alloy. The higher levels of strength are attributed to different strengthening mechanisms, such as load transfer to the hard dispersoid phase, enhanced dislocation density due to differential CTEs between matrix and secondary phase, and strengthening arising from constrained plastic flow [54].

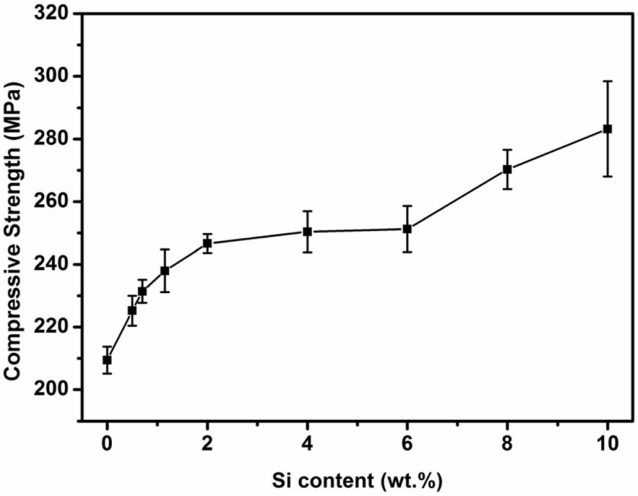

Fig. 19 Compressive strength of Mg-Si alloy with respect to Si content

The continuous interface observed in the fracture surface is also responsible for the increase in compressive strength. The fracture of Mg with high Si content occurs severely in Mg_2Si rich regions, which is due to the high local stresses caused by a restriction of the plastic zone surrounding neighbouring particles. This can be strongly influenced by the mutually interactive factors of the following: (a) local plastic constraint, (b) particle size and (c) degree of particle agglomeration. In addition, the increased local stress arising from a high volume fraction of particles facilitates rapid linkage [55]. Compared to tensile properties, the compressive properties show a different trend with Si additions. UTS of Mg-Si alloys increases up to 2 % Si addition and then decreases with further Si additions: whereas, the UCS values of the Mg-Si alloys are found to increase with the increase in Si content. The reason for the discrepancy is attributed to the difference in the deformation modes during tensile and compression. An increase in Si addition leads to more volume of Mg_2Si particles in the Mg matrix which increases the stress concentration resulting in the formation and propagation of cracks at the interface between the Mg_2Si and matrix during tensile loading. In contrast, crack formation and propagation are retarded during compression loading.

4 Conclusions

The microstructure and mechanical properties of pure Mg and different hypo as well as hypereutectic Mg-Si (Mg-0.5, 0.7,

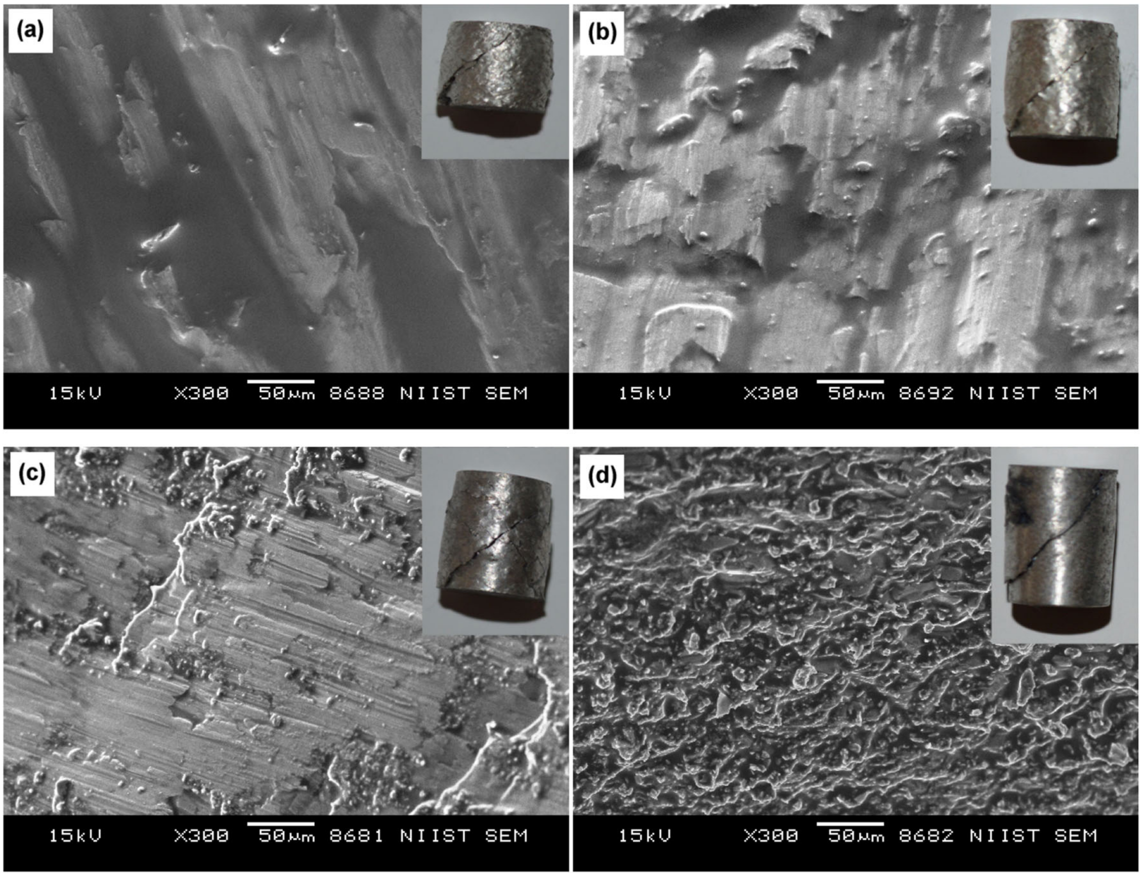

Fig. 20 Compressive fractographs of Mg-Si alloys (**a**) pure Mg, (**b**) Mg-1.15Si, (**c**) Mg-6Si and (**d**) Mg-10Si

1.15, 2, 4, 6, 8, and 10Si) alloys were investigated and the conclusions were as follows.

1. The microstructures of hypoeutectic Mg-Si alloys (Mg - 0.5, 0.7 and 1.15Si) were consisting of α-Mg dendrites and lamellar Mg_2Si phase. With the increase of Si content, the amount of the eutectic Mg_2Si phase increased and became coarser and continuous. However, the amount of α-Mg phase decreases as the Si content increases.
2. The microstructures of hypereutectic Mg-Si alloys (Mg - 2, 4, 6, 8 and 10Si) were having the phases such as primary Mg_2Si, α-Mg and eutectic Mg_2Si. With the increase of Si content, the morphology of eutectic Mg_2Si changes from a long needle, Chinese script type structure, into a small tiny needle shape structure. The amount of eutectic Mg_2Si decreases with an increase in Si content in the hypereutectic alloys. Similarly, the volume percentage of primary Mg_2Si increases with an increase in Si content in the alloys and its morphology changes from polygonal to coarse dendritic structure.
3. The hardness value increases steadily with an increase in Si content. The enhancement in hardness was due to the presence of hard Mg_2Si intermetallic phase with the Si additions. The microhardness measurement revealed that α-Mg has less hardness, comparable to that of pure Mg. The eutectic Mg-Mg_2Si region yields comparatively higher hardness than α-Mg in both the hypo and hypereutectic alloys. In the hypereutectic alloys, the primary Mg_2Si phase exhibits the highest hardness among all other constituents. The average microhardness of primary Mg_2Si was about 10 times higher than that of α-Mg.
4. The UTS value increases up to 2 % Si addition, beyond that it decreases. The results show that Mg with 2 and 4 % Si exhibit, better tensile properties. The maximum YS was obtained at 6 % Si and beyond that marginal reduction was observed. The uniform distribution of the fine eutectic and primary Mg_2Si in the Mg matrix was attributed to the improvement in strength properties. The reduction in strength obtained with 4Si addition and beyond was due to the presence of the high volume coarse dendritic primary Mg_2Si phase.
5. The elevated temperature strength properties of these alloys decrease with an increase in the test temperature from RT to 150^{o}C, especially with low Si-containing alloys. In high Si content (Mg - 6, 8 and 10Si) alloys, the reduction in strength is very marginal which is due to the presence of the high volume of thermally stable primary Mg_2Si phase in high Si containing alloys.
6. The ultimate compressive strength (UCS) values of Mg-Si alloys were found to increase significantly with Si content. This increase is due to the presence of the hard intermetallic Mg_2Si phase which shared the major load from the matrix.

Acknowledgements The author wishes to acknowledge the Council of Scientific and Industrial Research [CSIR], Govt. of India and to thank the casting and characterization facilities provided by MatRICS – Materials Research and Innovation Centric Solutions, Vellimalai, Kanyakumari District, India, Tel: +91 91766 06699; web: www.matricstech.com. The help received from Mr. Hari Krishnan, Mr. Ajukumar, Mr. S. Prasanth and Mr. Abhilash Viswanath during the experiments is highly acknowledged.

Authors Contribution K.K. Ajith Kumar, A Srinivasan, U. T. S. Pillai, B C. Pai and M. Chakraborty contributed to the design, implementation of the research and for preparing the manuscript.

Research involving human participants and/ or animals: Not Applicable.

Data Availability All the original data are available with the corresponding author.

Code Availability Not applicable.

Declarations

Conflict of Interest The authors declare that they have no conflicts of interest.

Ethics Approval Not applicable.

Consent to Participate Not applicable.

Consent for Publication Publishers can publish images and results there are no restrictions.

References

1. Mordike BL, Ebert T (2001) Magnesium: Properties — applications — potential. Mater Sci Eng A 302(1):37–45
2. Ostrovsky I, Henn Y (2007) Present state and future of magnesium application in aerospace industry, ASTEC'07 International Conference- New Challenges in Aeronautics 1-5
3. Ye H, Liu X (2004) Review of recent studies in magnesium matrix composites. J Mater Sci 39(20):6153–6171
4. Brown RE (2009) Magnesium in the 21st century. Adv Mater Process 167(1):31–33
5. Chen ZH, Chen JH (2008) A review: Hot topics on magnesium technology in China. Front Mater Sci Chin 2(1):1–8
6. Luo AA (2002) Magnesium: Current and potential automotive applications. JOM 54(2):42–48
7. Caceres CH (2006) Light alloy castings for automotive applications: The case of Al vs. Mg, 10th International Conference on Aluminium Alloys, 1801-1808.
8. Carbonneau Y, Couture A, Van Neste A, Tremblay R (1998) On the observation of a new ternary MgSiCa phase in Mg-Si alloys. Metall Mater Trans A 29(6):1759–1763
9. Friedrich HE, Mordike BL (2006) Magnesium technology: metallurgy, design data, applications. Springer, Berlin
10. Wang HY, Zhang EB, Nan XL, Zhang L, Guan ZP, Jiang QC (2016) A comparison of microstructure and mechanical properties

of Mg–9Al–1Zn sheets rolled from as-cast, cast-rolling and as-extruded alloys. Mater Des 89:167–172

11. Turen Y (2013) Effect of Sn addition on microstructure, mechanical and casting properties of AZ91 alloy. Mater Des 49:1009–1015
12. Murugan G, Raghukandan K, Pillai UTS, Pai BC, Mahadevan K (2009) High cyclic fatigue characteristics of gravity cast AZ91 magnesium alloy subjected to transverse load. Mater Des 30(7): 2636–2641
13. Li G, Jiang W, Yang W, Jiang Z, Guan F, Jiang H, Fan Z (2019) New insights into the characterization and formation of the interface of A356/AZ91D bimetallic composites fabricated by compound casting. Metall Mater Trans A 50(2):1076–1090
14. Praveen TR, Gopi KR, Nayaka HS (2018) Numerical simulation of shot peening process on equal channel angular pressed magnesium alloy. Silicon 10:2463–2472
15. Praveen TR, Nayakaa HS, Swaroop S (2019) Influence of equal channel angular pressing and laser shock peening on fatigue behaviour of AM80 alloy. Surf Coat Technol 369:221–227
16. Praveen TR, Nayaka HS, Swaroop S, Gopi KR (2020) Strength enhancement of magnesium alloy through equal channel angular pressing and laser shock peening. Appl Surf Sci. https://doi.org/10.1016/j.apsusc.2020.145755
17. Zhang Z, Jiang W, Li G, Wang J, Guan F, Jie G, Fan Z (2021) Improved interface bonding of Al/Mg bimetal fabricated by compound casting with Nd addition. Mater Sci Eng A 826:141998. https://doi.org/10.1016/j.msea.2021.141998
18. Powell BR, Rezhets V, Balogh MP, Waldo RA (2001) The relationship between microstructure and creep behavior in AE-42 magnesium die casting alloy, pp 175–181
19. Pekguleryuz MO, Renaud J (2000) Creep resistance in Mg-Al-Ca casting alloy, 279-284
20. Luo AA (2004) Recent magnesium alloy development for elevated temperature applications. Int Mater Rev 49(1):13
21. Pettersen G, Westengen H, Hoier R, Lohne O (1996) Micro structure of a pressure die cast magnesium-4wt. % aluminium alloy modified with rare earth additions. Mater Sci Eng A 207(1):115–120
22. Shabadi R, Ambat R, Dwarakadasa ES (2014) AZ91C magnesium alloy modified by Cd. Mater Des 53:445–451
23. Zafari A, Ghasemi HM, Mahmudi R (2014) An investigation on the tribological behavior of AZ91 and AZ91 + 3 wt% RE magnesium alloys at elevated temperatures. Mater Des (1980-2015) 54: 544-552
24. Ben-Hamu G, Eliezer D, Kaya A, Na YG, Shin KS (2006) Microstructure and corrosion behavior of Mg–Zn–Ag alloys. Mater Sci Eng A 435–436:579–587
25. Mendis CL, Oh-ishi K, Hono K (2007) Enhanced age hardening in a Mg–2.4at.% Zn alloy by trace additions of Ag and Ca. Scripta Mater 57(6):485-488
26. Movahedi-Rad A, Mahmudi R (2014) Effect of Ag addition on the elevated-temperature mechanical properties of an extruded high strength Mg–Gd–Y–Zr alloy. Mater Sci Eng A 614(0):62–66
27. Qi FG, Zhang DF, Zhang XH, Pan FS (2014) Effect of Y addition on microstructure and mechanical properties of Mg–Zn–Mn alloy. Trans Nonferrous Met Soc China 24(5):1352–1364
28. Wu L, Cui C, Wu R, Li J, Zhan H, Zhang M (2011) Effects of Ce-rich RE additions and heat treatment on the microstructure and tensile properties of Mg–Li–Al–Zn-based alloy. Mater Sci Eng A 528(4–5):2174–2179
29. Zhang JS, Sun Y, Cheng WL, Que ZP, Li YM, Liushan L (2013) The effect of Ca addition on microstructures and mechanical properties of Mg-RE based alloys. J Alloys Compd 554(0):110–114
30. Qu Z, Wu L, Wu R, Zhang J, Zhang M, Liu B (2014) Microstructures and tensile properties of hot extruded Mg–5Li–3Al–2Zn–xRE (Rare Earths) alloys. Mater Des. 54(0):792–795
31. Liao L, Zhang X, Wang H, Li X, Ma N (2007) Influence of Sb on damping capacity and mechanical properties of Mg2Si/Mg–9Al composite materials. J Alloys Compd 430(1–2):292–296
32. Mabuchi M, Higashi K (1996) Strengthening mechanisms of Mg-Si alloys. Acta Mater 44(11):4611–4618
33. Chen K, Li ZQ, Liu JS, Yang JN, Sun YD, Bian SG (2009) The effect of Ba addition on microstructure of in situ synthesized Mg_2Si/Mg-Zn-Si composites. J Alloys Compd 487(1–2):293–297
34. Jiang QC, Wang HY, Wang Y, Ma BX, Wang JG (2005) Modification of Mg_2Si in Mg-Si alloys with yttrium. Mater Sci Eng A 392(1–2):130–135
35. Li GH, Gill H, Varin R (1993) Magnesium silicide intermetallic alloys. Metall Mater Trans A 24(11):2383–2391
36. Wang HY, Li Q, Liu B, Zhang N, Chen L, Wang JG, Jiang QC (2012) Modification of primary Mg_2Si in Mg-4Si alloys with antimony. Metall Mater Trans A 43(13):4926–4932
37. Hadian R, Emamy M, Campbell J (2009) Modification of cast Al-Mg_2Si metal matrix composite by Li. Metall Mater Trans B 40(6): 822–832
38. Bronfin B, Moscovitch N (2006) New magnesium alloys for transmission parts. Met Sci Heat Treat 48(11–12):479–486
39. Mabuchi M, Kubota K, Higashi K (1996) Tensile strength, ductility and fracture of magnesium-silicon alloys. J Mater Sci 31(6):1529–1535
40. Mabuchi M, Kubota K, Higashi K (1995) High strength and high strain rate superplasticity in an Mg-Mg_2Si composite. Scr Metall Mater 33(2):331–335
41. Okamoto H (2007) Mg-Si (Magnesium-Silicon). J Phase Equilib Diffus 28(2):229–230
42. Yan XY, Chang Y, Zhang F (2000) A thermodynamic analysis of the Mg-Si system. J Phase Equilib 21(4):379–384
43. Porter DA, Easterling KE (2004) Phase transformations in metals and alloys. Nelson Thornes, Cheltenham
44. Pan Y, Liu X, Yang H (2005) Microstructural formation in a hypereutectic Mg-Si alloy. Mater Charact 55(3):241–247
45. Li C, Wu YY, Li H, Liu XF (2011) Morphological evolution and growth mechanism of primary Mg_2Si phase in Al–Mg_2Si alloys. Acta Mater 59(3):1058–1067
46. Qin QD, Zhao YG (2008) Nonfaceted growth of intermetallic Mg_2Si in Al melt during rapid solidification. J Alloys Compd 462(1–2):L28–L31
47. Beer S, Frommeyer G (1992) Development of Mg-Mg_2Si light weight alloys. In: Mordike BL, Hehmann F (eds) Magnesium alloys and their application, 317-324
48. Emamy M, Jafari Nodooshan HR, Malekan A (2011) The microstructure, hardness and tensile properties of Al–15 %Mg2Si in situ composite with yttrium addition. Mater Des 32(8–9):4559-4566
49. Lu Y, Wang Q, Zeng X, Ding W, Zhai C, Zhu Y (2000) Effects of rare earths on the microstructure, properties and fracture behavior of Mg–Al alloys. Mater Sci Eng A 278(1–2):66–76
50. Hadian R, Emamy M, Varahram N, Nemati N (2008) The effect of Li on the tensile properties of cast Al–Mg2Si metal matrix composite. Mater Sci Eng A 490(1–2):250–257
51. Emamy M, Jafari Nodooshan HR, Malekan A (2011) The microstructure, hardness and tensile properties of Al-15 % Mg_2Si in situ composite with yttrium addition. Mater Des 32(8–9):4559–4566
52. Emamy M, Nemati N, Heidarzadeh A (2010) The influence of Cu rich intermetallic phases on the microstructure, hardness and tensile properties of Al–15 % Mg_2Si composite. Mater Sci Eng A 527(12): 2998–3004
53. Jayalakshmi S, Kailas SV, Seshan S (2002) Tensile behaviour of squeeze cast AM100 magnesium alloy and its Al_2O_3 fibre reinforced composites. Compos Part A Appl Sci Manuf 33(8):1135–1140
54. Kumar NVR, Dwarakadasa ES (1994) Fracture behaviour of Al-Zn-Mg/SiCp composites. J Mater Sci 29(6):1533–1539

55. Li JQ, Wang L, Cheng HW, Zhang HF, Hu ZQ, Cai HN (2008) Synthesis and compressive deformation of rapidly solidified magnesium alloy and composites reinforced by SiCp. Mater Sci Eng A 474(1–2):24–29
56. Batra RC, Wei ZG (2007) Instability strain and shear band spacing in simple tensile/compressive deformations of thermoviscoplastic materials. Int J Impact Eng 34(3):448–463
57. Wang TS, Hou RJ, Lv B, Zhang M, Zhang FC (2007) Microstructure evolution and deformation mechanism change in 0.98 C–8.3Mn–0.04 N steel during compressive deformation. Mater Sci Eng A 465(1–2):68–71
58. Paramsothy M, Hassan SF, Srikanth N, Gupta M (2009) Enhancement of compressive strength and failure strain in AZ31 magnesium alloy. J Alloys Compd 482(1–2):73–80
59. Dieter GE (1928) Mechanical metallurgy. McGraw-Hill Book Company, New York